Catena 233 (2023) 107511

Contents lists available at ScienceDirect

Catena

journal homepage: www.elsevier.com/locate/catena

Dynamics of subsurface soil erosion in a semiarid region: A time-series study of sinkhole area and morphology

Osher Rafaeli [a,*], Ariel Nahlieli [a], Tal Svoray [a,b]

[a] The Department of Environmental, Geoinformatics and Urban Planning Sciences, Ben-Gurion University of the Negev, Israel
[b] Department of Psychology, Ben-Gurion University of the Negev, Israel

ARTICLE INFO

Keywords:
Soil piping
Sinkhole
Subsurface soil erosion
Semiarid environment
Soil crack
Loess

ABSTRACT

Subsurface soil erosion causes irreversible damage to agricultural fields by generating elongated pipes and elliptical sinkholes that can further develop into rills and gullies. However, despite their severe consequences, there is still limited available quantitative information on spatiotemporal dynamics of soil pipes and sinkholes, especially in semiarid regions; evidence of subsurface erosion rates is based on a small number of time points during a sampling period that is usually limited to a few successive years. Here, temporal changes in sinkhole area, and their level of circularity and orientation were quantified over a decade (2010–2020), in loess-derived soils in the semiarid Negev desert, Israel. Data were measured using high-resolution aerial photographs (1 pixel = 15 cm length), and were related to high-temporal-resolution rainfall data. The results revealed that: (1) soil pipe collapse is related to early winter rainfall events more than to mid or end-of-winter events, possibly due to the development of annual herbaceous vegetation that shields the soil and increases its resistance to erosion; (2) sinkhole and soil pipe morphological development and orientation are related to the orientation of stream banks and the tension cracks developed along those banks; and (3) changes in sinkhole area are related to catastrophic rainfall events and not to gradually accumulated annual rainfall.

1. Introduction

Loess-derived soils are a valuable resource for agriculture in semiarid regions but are vulnerable to degradation (Cai, 2001; Li et al., 2020; Zhao et al., 2013; Zhu, 2012) and decreasing health and, consequently, to a reduction in the provision of agroecosystem services (Rinot et al., 2019). Studies have reported that water erosion processes (García-Ruiz, 2010; Uri and Lewis, 1998) can cause irreversible damage in agricultural fields, costing tens of billions of dollars per annum globally (Svoray, 2022).

Prominent among the various water erosion processes in agricultural catchments is the influence of gullying on soil degradation (Hoober et al., 2017; Svoray et al. 2012; Poesen et al., 2002). Current research considers surface water flow as the main cause for gullying (Castillo and Gómez, 2016; Valentin et al., 2005; Vanmaercke et al., 2021; Panagos and Katsoyiannis, 2019). However, the less studied) subsurface water and sediment flows have also been found to affect gully erosion and soil degradation (de Ploey et al., 1995; Poesen et al., 1996; Starkel, 2011). The presence of piping systems within an area significantly increases the vulnerability to the formation of new gullies (Kariminejad et al., 2021). Soil piping has the potential to contribute to various processes related to gully formation (Bernatek-Jakiel and Poesen, 2018). One possible outcome is the formation of new gullies following the collapse of soil pipes. Additionally, soil piping can also cause the deepening and widening of existing gully channels (Poesen, 2011).

The dearth of studies on subsurface water erosion stems primarily from the fact that its temporal quantification is difficult (Bernatek-Jakiel et al., 2017). Nevertheless, we know that the development and morphological features of soil pipes are generally affected by several factors, including topography, lithology, soil properties, climate, presence of vegetation, bioturbation and soil management (Chen et al., 2022; Faulkner, 2013; Gutiérrez et al., 1997; Jones et al., 1997; Parker and Jenne, 1967; Piccarreta et al., 2006; Romero Díaz and López Bermúdez, 1989; Verachtert et al., 2010).

While the factors recognized as contributing to acceleration of piping erosion such as silt-rich soils (Bernatek-Jakiel et al., 2020); high exchangeable sodium content (Kariminejad et al., 2023); dispersive soils and poorly structured soils (Faulkner, 2013; Pereyra et al., 2020); pasture land use (Verachtert et al., 2013; Verachtert et al., 2010); or a semiarid climate (Romero Díaz et al., 2009), the specific determinants of

* Corresponding author.
E-mail addresses: osherr@post.bgu.ac.il (O. Rafaeli), arielnah@post.bgu.ac.il (A. Nahlieli), tsvoray@bgu.ac.il (T. Svoray).

https://doi.org/10.1016/j.catena.2023.107511
Received 27 April 2023; Received in revised form 4 September 2023; Accepted 5 September 2023
Available online 23 September 2023
0341-8162/© 2023 Elsevier B.V. All rights reserved.

rate and orientation of piping expansion, and their effects on gullying hydrological connectivity in hillslopes and catchments, and sediment yields are less known.

The temporal dynamics of soil pipes has been related to high-intensity rainfall events. For example, Zhu (2003) reported that in the Loess Plateau of China, most piping inlets are initiated by a few catastrophic rainfall events, whereas other, smaller events do not substantially affect the piping process. In the Flemish Ardennes in Belgium, soil loss due to sinkhole initiation or piping roof collapse markedly increased after a major rainfall event, while remaining constant during the summer, characterized by small events (Verachtert et al., 2011). Furthermore, monitoring sinkhole dimensions and measuring their variations in area/volume over time showed seasonal relationships between cumulative or daily rainfall depth and variations in sinkhole dimensions (Bernatek-Jakiel et al., 2017; Verachtert et al., 2011; Zhu, 2003). Piping initiation has been shown to be correlated with the length of dry spells, with long dry periods potentially leading to the development of soil cracks due to shrinkage and expansion processes in clay minerals, especially in semiarid areas (Barendregt and Ongley, 1977; Jones, 2004; Jones and Cottrell, 2007; Nahlieli et al., 2022; Pereyra et al., 2020). Another notable observation from temporal studies of soil pipes in the Bieszczady Mountains (Bernatek, 2015; Bernatek-Jakiel et al., 2017; Bernatek-Jakiel and Wrońska-Wałach, 2018) and other regions (Löffler, 1974) is that vegetation can delay piping surface collapse.

However, despite this acquired knowledge, current research is still limited to individual soil pipes and to long periods of sampling with few temporal measurements or, alternatively, short periods with limited coverage of only a few events (Bernatek-Jakiel et al., 2017; Kariminejad et al., 2021; Verachtert et al., 2011; Zhu, 2003).

Further quantification of changes in sinkhole geometry and elongation has shown roof collapse when several sinkholes develop along a soil pipe, or when one sinkhole is enlarged by roof collapse (Bernatek, 2015; Verachtert et al., 2010). Observations of collapsed features have been conducted to provide information on the location and dimensions of soil pipe sinkholes (Bernatek-Jakiel et al., 2019; Wilson et al., 2015). The orientation of elongated collapsed features can also provide information on the morphology of the soil pipes that are hidden underneath, although this has not been investigated in previous studies.

These results call for further exploration of soil pipe dynamics using larger spatial and temporal datasets, which may contribute to a better understanding of soil piping and its rate of change on a seasonal scale, and its association with environmental–topographical characteristics; and to characterize sinkhole dynamics in relation to stream banks and tension soil cracks (Nahlieli et al., 2022, 2023), including sinkhole morphology and orientation. We therefore aimed to quantify spatio-temporal variations in sinkhole (i.e., pipes collapses) area and morphology in a loess-dominated semiarid area, at sub-meter spatial resolution and seasonal-scale observation.

The relationship between pipe erosion in the subsurface and the area loss of sinkholes and roof collapses is widely acknowledged in the literature (Bernatek-Jakiel and Poesen, 2018). However, it is important to note that the quantification of soil material washed out from the soil pipe was not conducted in this study. Nevertheless, as previously stated, pipes with a high erosion rate are expected to exhibit accelerated expansion of sinkholes and an increased likelihood of collapses (Verachtert et al., 2011).

Our aim involved two operational objectives: (1) examining the rate of change in sinkhole morphology over 10 hydrological seasons (2010–2020) and its relation to (a) accumulated rainfall depth and the occurrence of large rainfall events, and (b) environmental and topographical characteristics, including normalized difference vegetation index (NDVI), upslope contributing area, gradient of the contributing area, solar radiation, and stream bank elevation and gradient; (2) quantifying sinkhole morphology dynamics using (a) a 2D circularity index of sinkhole according to its major ellipse axis orientation relative to the stream bank, and (b) the relationship of sinkhole orientation to tension cracks initiated on the stream banks. Accomplishment of these two objectives was expected to provide a better understanding of the physical and geometrical factors controlling sinkhole variation over space and time at the studied site.

2. Study area

The study sites were the Besor and Asaf agricultural catchments in the northwestern Negev desert, near the village of Re'im and the archaeological site Tel Gamma, east of the Mediterranean Sea coastline of Israel (Fig. 1). The moderate topography of the study sites is characterized by an elevation range of 45–90 m above mean sea level with hillslopes tilted at a moderate gradient (1°–5°), although the slope gradient can be much steeper (45°–90°) in the stream banks. The climate is semiarid with mean annual rainfall of 292 mm. The rainy season begins in September and ends in May, and most of the rain occurs between November and March. Rainfall regime is characterized by sporadic, short rainfall events of varying intensities and dry spells between them (Wolman and Gerson, 1978; Yair and Kossovsky, 2002). The summers are dry and hot with mean daily air temperature of 27 °C (Israel Meteorological Service, n.d.).

In December 2013, the Middle East region experienced a significant cold snap commonly referred to as the "Alexa" winter storm. This weather event had a substantial impact on countries including Syria, Jordan, Israel, Lebanon, Turkey, and Egypt (Hochman et al., 2022). The onset of "Alexa" coincided with the beginning of the rainy season, specifically on December 13, and brought about exceptionally heavy rainfall that had not been observed in the past five decades. The accumulated precipitation during this period reached 184 mm, which accounted for approximately 75% of the average annual rainfall, all occurring within a span of four days. The storm was accompanied by low temperatures and strong winds, leading to severe flooding in various affected areas. This information is based on records from the Israel Meteorological Service.

Soils are classified as Late Pleistocene loess with a sandy loam/silt loam texture (Nachshon, 2016; Stavi and Argaman, 2016). In these predominantly aeolian soils, the water-driven sediment-transport rate is highly responsive to the aeolian soil-production mechanisms and therefore, may vary greatly in space and time at the hillslope and landscape scales of observation (Cohen et al., 2017). Therefore, a representation of many soil pipes is required.

Under these climatic and soil conditions, the dry spells between rainfall events can lead to soil shrinkage and swelling due to alternating wet and dry conditions. The clay and silt fractions, along with sodium accumulation, generally increase with depth and may impact aggregate stability. There is also a trend of decreasing concentration of the least mobile ions (Ca^{2+}, Mg^{2+}) with depth at some sites. Soil organic matter content decreases with depth and there is a significant correlation between organic matter and Ca^{2+} and Mg^{2+} concentration at the study site (Nahlieli et al., 2022). These measurements suggest that the subsoil in the region is vulnerable to water erosion. Piping and gully erosion were observed close to stream banks in previous studies and our field reconnaissance (Fig. 2).

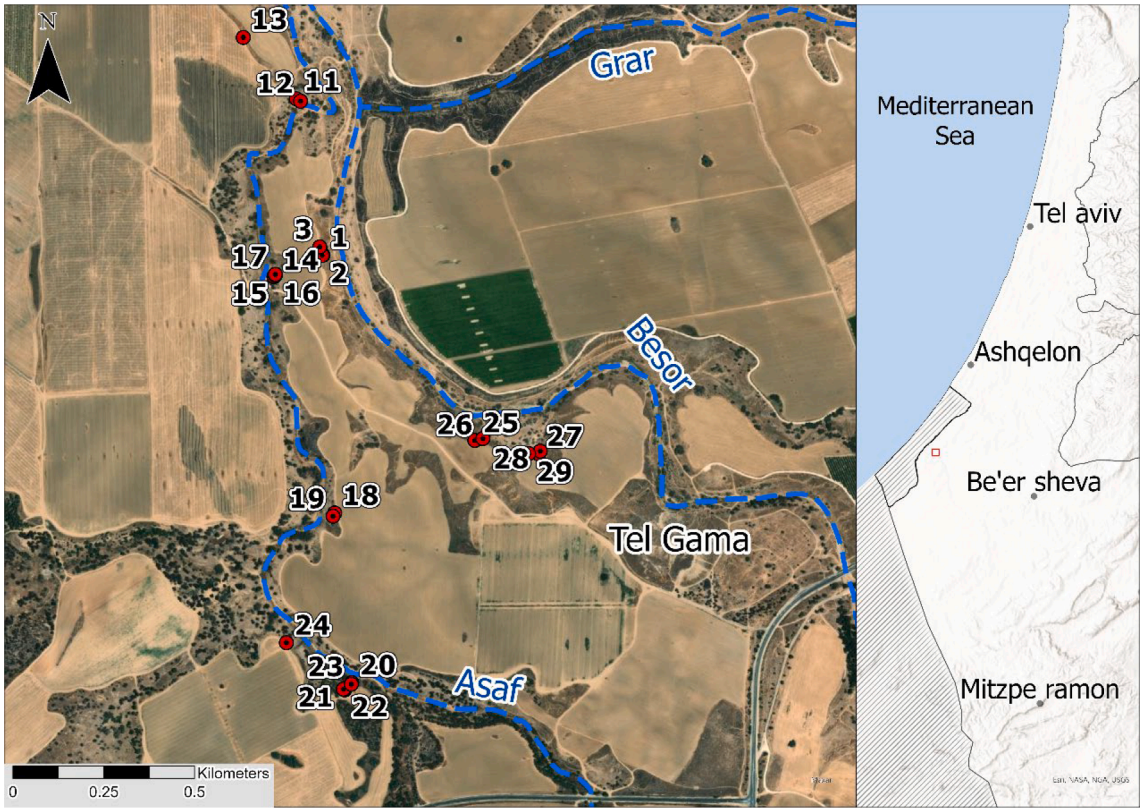

Fig. 1. The study area: Besor and Asaf catchments, located in the northwestern part of the Negev region, Israel. The orthophoto is overlapped by a point layer of the 1–29 sinkholes that were measured in the current research. Imagery Background map is from ESRI website, acquired by WV02 satellites updated to June 2021 provided by Maxar Technologies.

3. Methodology

We quantified subsurface erosion rates by monitoring changes in sinkhole area and geometry over time. The empirical evidence was derived from drone data and a historical series of high-resolution aerial photographs. The drone data were used to extract topographic and geospatial features (contributing area, contributing area slope gradient, solar radiation, distance to stream bank, stream bank elevation and gradient); the time-series analysis of aerial photos was used to quantify changes in the sinkholes' area over 10 hydrological seasons (2010–2020). Thus, the collection of 29 sinkholes caused by roof collapses of subsurface soil pipes included data on the following dependent variables for each sinkhole, at each time of acquisition of a given aerial photo: (1) sinkhole area; (2) circularity index using the Polsby–Popper test (PPT) (Polsby and Popper, 1991); and (3) orientation of sinkholes with reference to the nearest stream bank. The independent variables were: rainfall depth, geospatial variables and vegetation cover. The sinkhole area obtained from ariel photography is overlaid by daily rainfall recorded at the study site, in addition, the sinkholes time series provides an illustration of the sinkhole polygon circularity index (CI) at different dates. Through an initial visual inspection of the data, it became evident that there is a trend that indicates a consistent increase in the sinkhole area, while the CI value decreases. Notably, the most significant expansion in sinkholes occurs after the December 2013 storm (see an example for a given sinkhole in Fig. 3).

3.1. Rate of change in sinkhole area on a seasonal scale (dependent variable)

To quantify area loss due to piping processes, a time series (2010–2020) of 16 high-spatial-resolution (15 cm length per pixel) aerial photographs were used. We utilized a series of aerial photographs obtained from the archive of The Geographic Information Laboratory at Ben-Gurion University (BGU). These photographs were sourced from the Israeli Ministry of Agriculture & Rural Development. Sinkhole area loss was therefore examined using fifteen time steps. These time steps correspond to the intervals between the dates when aerial photographs were captured. The aerial photographs were acquired prior to and following the wet season, typically occurring between the months of November and March. This time steps enabled a comprehensive assessment of the sinkhole area throughout the entire wet season. Additionally, a more detailed examination was performed within a specific season, focusing on a narrower time steps. It should be noted that the air photos that were captured at the end of each time step were utilized as references for the subsequent time steps. As a result, we were able to cover 15 time steps using only 16 photographs. The absence of area change in sinkholes during the dry season, is demonstrated both globally (Verachtert et al., 2011) and in our research area (Nahlieli et al.,

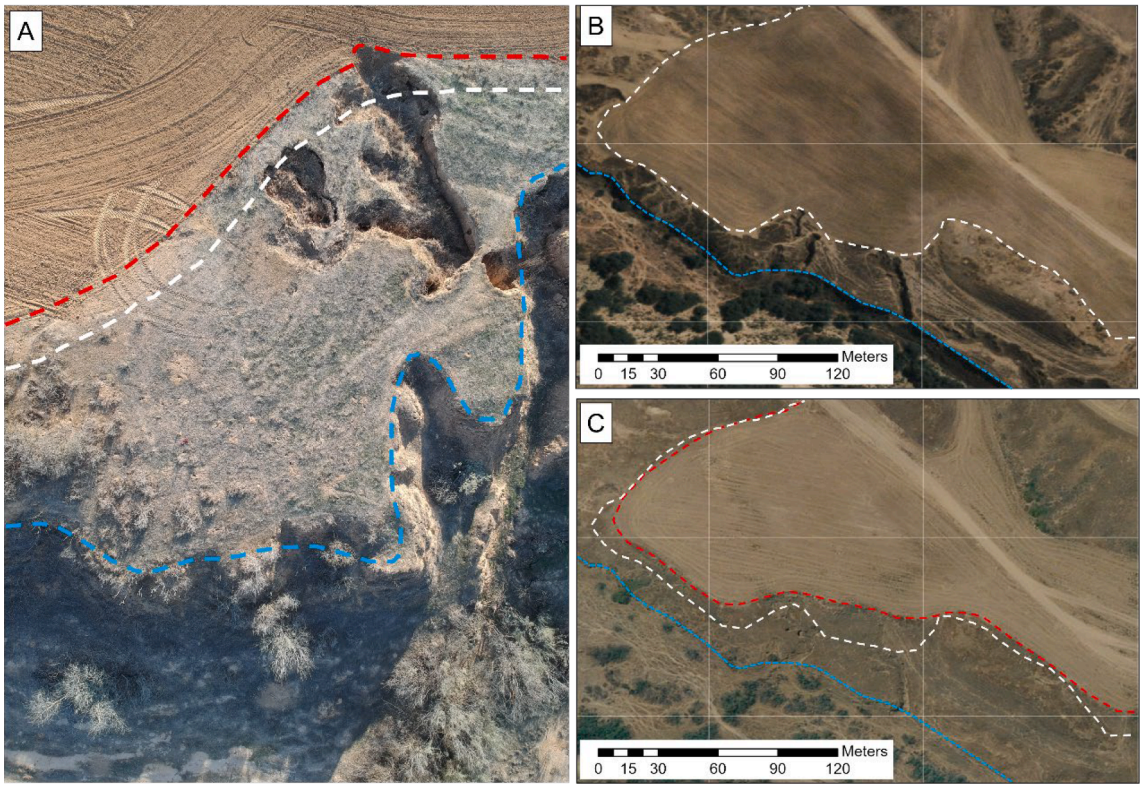

Fig. 2. (A) Drone image of an agricultural field located on the Besor stream bank damaged by piping erosion. (B) Aerial photo of agricultural fields in the study site in 2010. (C) Aerial photo of agricultural fields in 2018. Dashed blue line represents the stream bank in the three images. Dashed white line represents the border between the abandoned area (due to piping damage) and the cultivated area in 2010. Dashed red line represents the border between the abandoned area and the cultivated area in 2018. Note that due to piping processes, a large area was withdrawn from the cultivation cycle. Aerial photos from the Survey of Israel website. (For interpretation of the references to colour in this figure legend, the reader is referred to the web version of this article.)

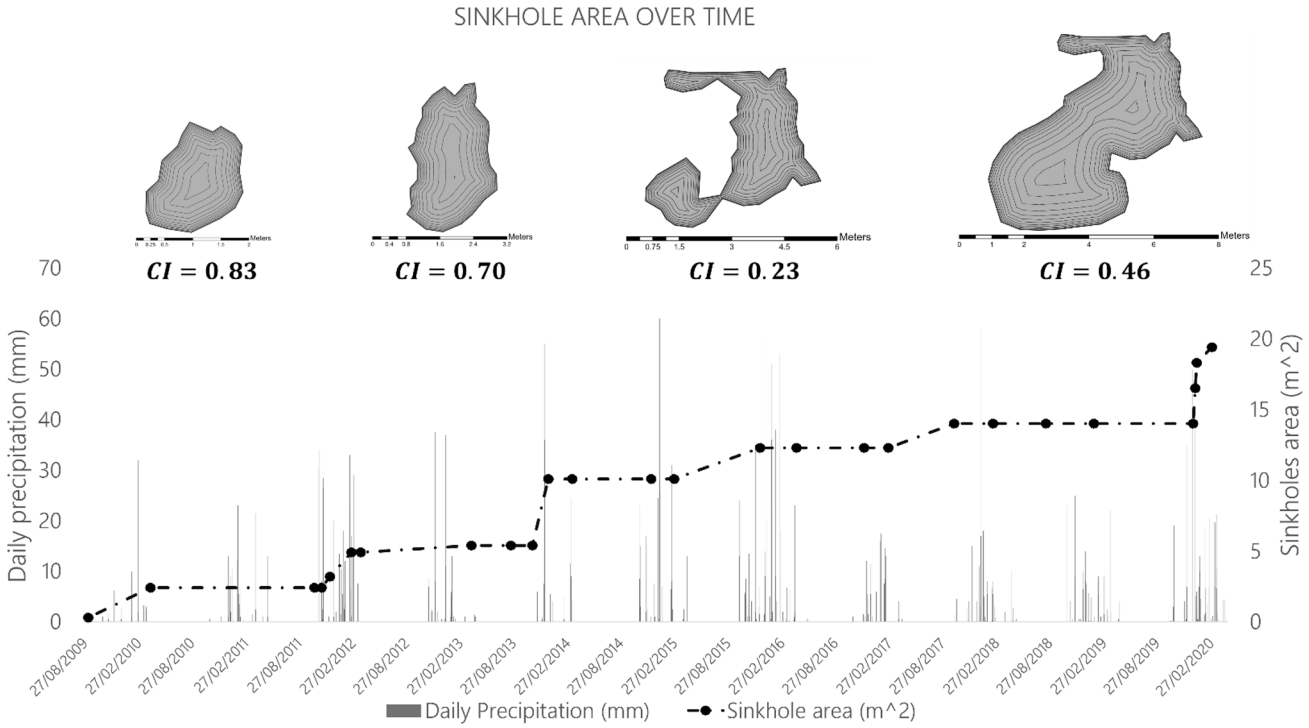

Fig. 3. Illustration of the evolution of a single sinkhole (#25) from August 2009 until March 2020 (location: Besor catchment). The sinkhole evolution is overlaid by daily rainfall recorded at the study site. Time series of sinkholes area represents area obtained from aerial photography, overall, 16 dates.

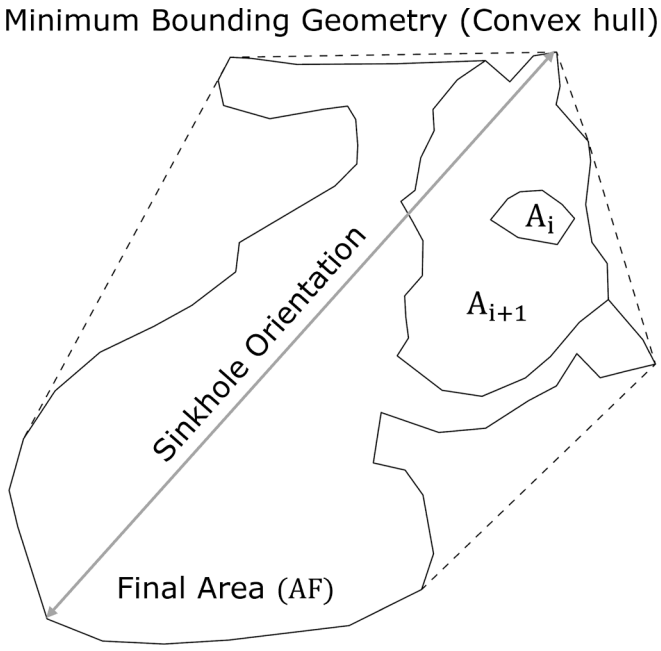

Fig. 4. Example of digitized sinkhole #25, showing three sinkhole stages at different time steps: the measured sinkhole area at certain time (A_{i+1}), at the previous time (A_i), and at the last sampling time (Final Area). The minimum bounding geometry was calculated on the final area with a line between the two most distant vertices (orientation of the sinkhole).

2023) and occurs because of lack of rainfall and infiltration in this season. This approach provided a consistent basis for evaluating sinkholes area change over time. Measurements were based on visual orthophoto interpretation and a field survey for validation using an Arrow 100 differential GPS device (with ~ 30 cm accuracy) to improve their positional accuracy. Sinkhole boundaries were digitized using ArcGIS PRO. Due to the high spatial resolution of the aerial photos, the sinkhole boundaries were very clear, with no doubts cast on their interpretations by the authors.

Sinkhole geometry was obtained during its enlargement (further collapse) until it is developed into a new gully or joined an existing gully. In such locations, the sinkhole was digitized from the year it first appeared or the first photo that covered it, until collapse. The result of this step was a time series of sinkhole areas (A_i) and the area loss index:

$$\text{Area loss index}\ (\%) = \frac{A_{i+1} - A_i}{AF} * 100 \quad (1)$$

where A is the sinkhole area in cm^2, i is the time index, i.e., the time of the given aerial photo, and $i + 1$ is the later adjacent aerial photo. AF is the area of the sinkhole in the latest year (Fig. 4). The area loss index is used to normalize changes in sinkhole dimensions, thereby allowing comparisons between sinkholes.

3.2. Sinkhole morphology

For the geometrical characterization of the shape of the 29 sinkholes, we used the standard definition of the circularity index (Polsby and Popper, 1991; Eq. (2). The PPT is a classical and popular circularity contour-based index (Nagy and Szákal, 2020). It compares the shape of the studied polygon to the area of a circle O that has the same perimeter size as the shape. The computed value of the circularity index will therefore be 1 for a sinkhole with a perimeter in the shape of a perfect circle, and it will decrease toward zero for noncircular polygons (Fig. 3). This index is suited to our analysis because noncircular features of sinkholes can indicate the orientation of subsurface pipes (Bernatek, 2015).

The circularity index was computed for each of the 29 sinkholes at each of the 16 sampling dates from the time that the sinkhole appeared in the aerial photo to the time of its collapse.

$$\text{Circularity index} = \frac{4\pi * Area}{Perimeter^2},\ 1 \rightarrow \text{Perfect circle} \quad (2)$$

The orientation of the elliptical sinkholes was calculated in two steps (Kobal et al., 2015): (1) the minimum bounding geometry tool of ArcGIS

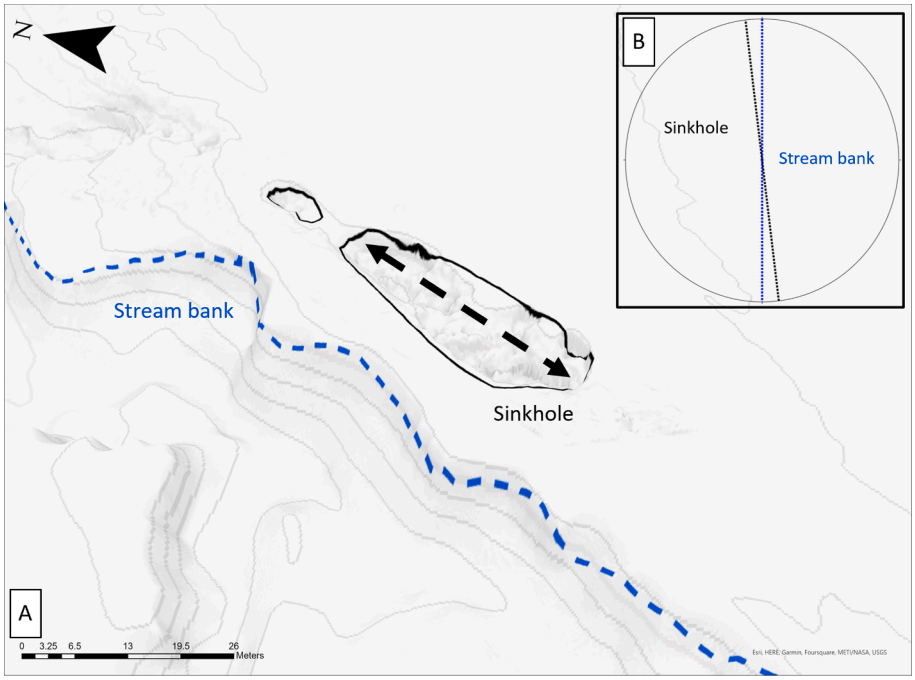

Fig. 5. (A) 3D view of stream bank and sinkhole. (B) 2D view of the stream bank's (blue line) and sinkhole's (black line) major axes. This representation was applied to 29 sinkholes and each sinkhole was related to the referenced stream bank. (For interpretation of the references to colour in this figure legend, the reader is referred to the web version of this article.)

PRO was executed to create convex hull polygons around the sinkhole features and to calculate the line between the two most distant polygon vertices (Fig. 4). This line has some orientation relative to north, which represents the orientation of the major dimension of the sinkhole feature in our analysis; (2) we calculated the angle between the stream bank line and the major axis of the sinkhole. An angle of 0° indicates that the two axes have the same orientation (parallel), and a 90° angle means that they are perpendicular. The relative orientation to the stream bank was computed to determine whether the sinkhole is parallel or perpendicular to the stream bank and in particular, to the tension cracks that exhibit a parallel or nearly parallel to the stream bank boundary direction based on a recent study in the site (Nahlieli et al. 2022). As already noted, the orientation of the sinkholes indicates the orientation of the collapsing subsurface pipe (Fig. 5).

3.3. Rainfall data

Rainfall depth data (in mm) for each time step, and accumulated rainfall data, were computed from continuous rainfall measurements extracted from the nearby standard meteorological station at Kisufim, located 3 km (aerial distance) from the sinkhole study site (source: Israel Meteorological Service).

3.4. Geospatial features

To simulate the study site topography and geomorphometry, it was photographed using an unmanned aerial vehicle (UAV)—DJI Phantom 4 RTK, carrying a 12 MP RGB camera to create high-resolution images. Agisoft Metashape® software was used for photogrammetry of the drone output images: (1) high-resolution orthophotos with spatial resolution of 2 cm per pixel; and (2) a digital surface model (DSM) with spatial resolution of 6 cm per pixel. From these two products, we calculated the following six geospatial variables using the spatial analyst tool of ArcGIS Pro: upslope contributing area (m^2), upslope contributing area slope gradient (^{o}), solar radiation (Wh/m^2), distance to stream bank (m), stream bank elevation above the channel bottom (m) and gradient (computed as stream bank height [m]/distance to stream bank [m]).

3.5. Vegetation data

Mean NDVI values were computed using Landsat TM 4–9 for all sinkhole locations within 1 week before or after the studied rainfall events. All Landsat TM images were obtained from the US Geological Survey (USGS) Earth Explorer, using Collection 2 (C2) Level 2 Science Products (L2SP) that were atmospherically and radiometrically corrected to surface reflectance by the USGS and Earth Resources Observation and Science (EROS) tools (Masek et al., 2006; Vermote et al., 2016). Mean NDVI values of the area closest to the sinkhole (30 m neighborhood) were used to estimate the increase in surface coverage of annual herbaceous plants at the studied site (Svoray and Shoshany, 2004). Herbaceous vegetation typically covers large parts of the area from the end of January to mid-March. Toward the summer, it begins to wilt and die off (Argaman et al., 2020).

3.6. Statistical analysis

We used ordinary least squares regression analyses to test statistical correlations between area changes for each time step (dependent variable, computed by Eq. (1) and each geospatial variable from section 3.4 (as independent variables). The number of observations of area changes equaled the number of sinkholes (29) over 15 time steps (n = 435) and the six environmental independent variables.

4. Results

4.1. Rate of change in sinkhole area on a seasonal scale

The mean increase in sinkhole area for all 29 sinkholes at all time steps was 9.5 m^2, and the mean size of the sinkholes at the last observation point was 11 times larger than the mean size of their initial area in 2010. The overall area of the 29 sinkholes increased by 280 m^2 during this period, and their associated seasonal area loss ranged from 0 to 48 m^2 in a single season, with a mean area loss index in a single season of ~ 7%. None of the sinkholes remained stable during the entire 10-season period. It is important to acknowledge that, systematic measurement of sinkhole depth was not consistently conducted in our study. However, during the field survey, we measured a subset of sinkholes and observed a range of depths, varying from 20 cm to 3 m. Most of the measured sinkholes varied within the range of 50–100 cm.

Table 1 reports the area loss for the 29 sinkholes throughout the 10-year study period. A weak positive correlation was observed between maximum total rainfall depth per event and area loss (n = 15, $R^2 = 0.56$, $P < 0.000$). In addition, a weak positive correlation was observed between accumulated rainfall for time step and area loss ($R^2 = 0.30$, $P < 0.000$). An exploration of the changes in sinkhole area close to the occurrence of extreme events revealed that the December 2013–2014 “Alexa” storm event widened almost all of the sinkholes (21 out of 23 on that date), with an average increase of 37% of their area before the

Table 1
Summary of sinkhole area changes.

Time step				Area loss index				Max rainfall event			
Start (dd/mm/yy)	End (dd/mm/yy)	Season	Accumulated Rainfall (mm)	Mean (%)	Max (%)	Min (%)	SD (%)	Depth (mm)	Start (dd/mm/yy)	End (dd/mm/yy)	Mean NDVI
27/01/09	10/04/10	09–10	223	1%	11%	0%	3%	51	25/02/10	28/02/10	0.27
10/04/10	20/10/11	10–11	207	5%	51%	0%	11%	69	30/01/11	01/02/11	0.14
20/10/11	13/11/11	11–12 A	157	8%	47%	0%	14%	62	03/11/11	04/11/11	0.06
13/11/11	12/12/11	11–12B	177	17%	74%	0%	21%	80	16/11/11	20/11/11	NO DATA
12/12/11	23/02/12	11–12C	85	2%	25%	0%	6%	42	01/03/12	02/03/12	NO DATA
26/03/12	07/04/13	12–13	182	5%	33%	0%	9%	60	08/01/13	10/01/13	0.12
07/04/13	25/12/13	13–14 A	219	37%	100%	0%	27%	184	10/12/13	14/12/13	0.12
25/12/13	16/03/14	13–14B	91	0%	0%	0%	0%	52	11/03/14	14/03/14	0.26
16/03/14	26/02/15	14–15	436	1%	6%	0%	2%	161	06/01/15	10/01/15	0.24
26/02/15	16/12/15	15–16 A	202	2%	14%	0%	4%	40	30/11/15	03/12/15	0.24
16/12/15	18/04/16	15–16B	403	6%	89%	0%	20%	126	22/01/16	27/01/16	0.32
18/04/16	07/10/17	16–17	189	2%	13%	0%	4%	59	11/02/17	16/02/17	0.31
07/10/17	16/02/18	17–18	202	2%	15%	0%	4%	78	04/01/18	06/01/18	0.19
16/02/18	26/01/19	18–19	256	0%	0%	0%	0%	34	22/11/18	23/11/18	0.15
26/01/19	03/03/20	19–20	445	11%	95%	0%	25%	58	26/12/19	27/12/19	0.16

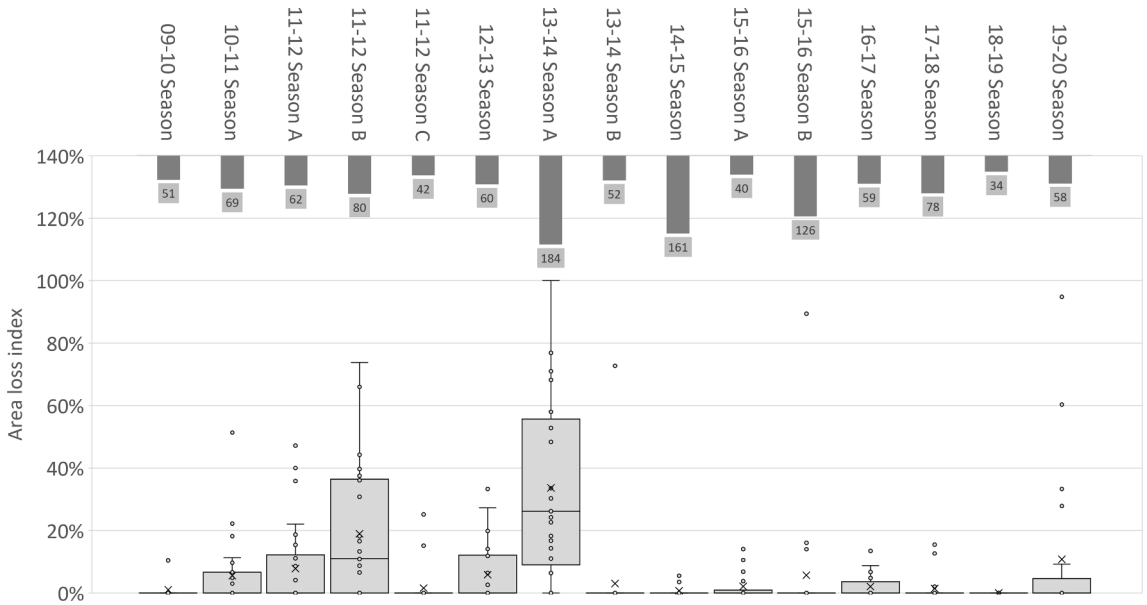

Fig. 6. Box-and-whisker plot of all sinkholes' area loss index for each season, with maximum storm rainfall depth during the time step (in the upper part of the diagram). The reduction in sinkhole area changes after 13–14 season A (184 mm) "Alexa" storm.

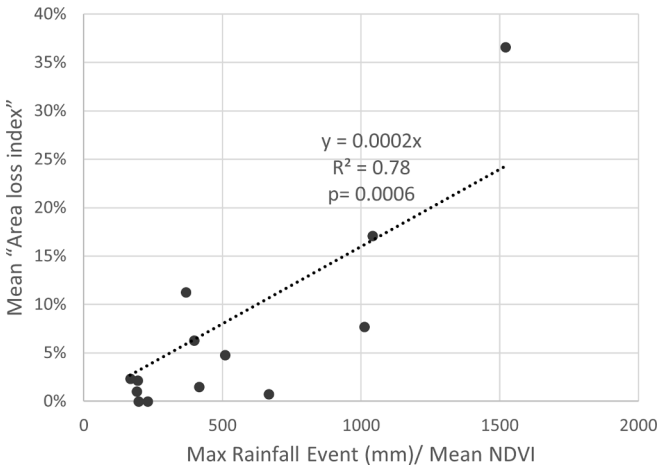

Fig. 7. A strong relationship is observed between sinkholes' mean area loss index and rainfall event depth (mm) divided by mean NDVI.

event. A significant change in sinkhole area was also detected during the early events of November 2011. Both events (3–4 Nov with rainfall of 62 mm depth and 16–20 Nov with rainfall of 79.5 mm depth [Israel Meteorological Service]) resulted in the widening of 21 sinkholes, with average increases of 8% and 17% in area for each rainfall event, respectively.

Conversely, three stable periods were observed during the seasons following the December 2013 "Alexa" storm, even though these seasons were characterized by significant rainfall events: the 2014–15 season, 2015–16 season and 2017–18 season (Fig. 6). This may have been due to a lack of available unstable soil material for transportation after the massive collapse in the earlier rainfall events.

NDVI data were added as an independent variable to the regression analysis by dividing rainfall depth by NDVI per event. This ratio represents a proxy for the potential of soil pipes to collapse in each rainfall event. While rainfall event total depth (in the denominator) increases the potential of pipe collapse and area loss, the presence of herbaceous plants (in the numerator) decreases it due to increased soil resistance to erosion (de Baets et al., 2006, 2008; Gyssels et al., 2005). The additional NDVI data greatly improved the coefficient of determination, from $R^2 = 0.56$ to $R^2 = 0.78$, and the significance level to $P < 0.000$.

Higher NDVI values, representing higher vegetation cover, were observed during the wet season (Fig. 7). This is because the NDVI of annuals reaches high values (and vegetation cover) at the study site after only 2–3 months of water supply from rainfall. This appeared to affect area loss. For example, rainfall events during the January 2014–15 and 2015–16 seasons showed only minor sinkhole area spread, with the area loss index increasing by 1% and 6%, respectively. This low response in terms of area loss may be because at this point in the season, the herbaceous vegetation is more developed compared to that in the November–December rainfall events in the 2011–12, 2013–14 and 2019–20 seasons.

Finally, it is important to note that for each sinkhole location, geospatial characteristics—upslope contributing area, slope gradient of contributing area, stream bank height, distance from the stream bank, gradient, and solar radiation at the stream bank—did not show a strong relationship with area loss rates in the sinkholes (Table 2).

Table 2
Summary table of sinkholes' geospatial characteristics extracted from DSM. No relationship was observed between total area loss, area loss during the "Alexa" storm and geospatial characteristics.

	Total area loss (m^2)	"Alexa" storm area loss (m^2)	Contributing area (m^2)	Contributing area slope gradient (°)	Solar radiation on stream bank (Wh/m^2)	Distance to stream bank (m)	Stream bank elevation above stream (m)	Gradient
S1	7.2	4.5	0.5	12.5	172576.5	26.9	9.3	0.3
S2	1.1	0.0	0.3	13.9	172576.5	29.5	10.2	0.3
S3	3.7	2.8	0.3	26.2	172576.5	32.6	9.0	0.3
S4	3.4	2.5	1.8	7.8	397856.0	5.0	5.5	1.1
S5	9.9	4.8	0.1	0.0	397856.0	6.4	5.9	0.9
S6	5.6	5.6	0.4	2.5	223480.2	18.2	4.2	0.2
S7	22.8	22.8	0.2	8.5	157110.5	3.6	4.2	1.1
S8	43.6	4.8	0.1	8.8	263406.5	20.5	5.2	0.3
S9	3.7	0.0	0.3	4.3	263406.5	0.0	3.0	–
S10	17.0	1.2	0.4	0.0	263406.5	5.7	5.8	1.0
S11	2.4	0.6	0.1	1.4	392751.7	6.7	6.7	1.0
S12	0.5	0.0	0.3	14.9	392751.7	0.1	6.0	67.5
S13	7.1	3.9	0.3	4.2	309331.5	2.6	3.4	1.3
S14	5.2	0.0	0.5	19.7	290994.7	10.0	2.4	0.2
S15	0.1	0.0	0.8	3.1	290994.7	13.6	2.7	0.2
S16	0.1	0.0	0.5	20.5	290994.7	13.4	2.8	0.2
S17	0.3	0.0	0.5	3.8	290994.7	13.6	3.4	0.3
S18	49.3	38.2	1.1	5.0	413651.4	18.4	4.8	0.3
S19	2.5	0.0	2098.6	2.7	413651.4	11.6	4.8	0.4
S20	32.7	24.3	0.9	1.9	214753.9	7.3	2.4	0.3
S21	5.1	1.4	0.1	7.3	214753.9	33.8	2.7	0.1
S22	1.5	0.2	0.1	6.5	214753.9	34.4	2.7	0.1
S23	2.8	2.0	8540.8	6.4	214753.9	11.6	2.4	0.2
S24	10.4	0.0	0.3	3.4	254104.6	33.1	1.9	0.1
S25	19.1	4.7	1.6	3.5	168400.0	27.5	7.5	0.3
S26	6.0	0.0	0.6	3.3	168400.0	10.6	8.3	0.8
S27	7.0	1.2	0.3	5.0	163076.2	8.4	7.1	0.8
S28	1.7	0.7	1.1	3.3	163076.2	7.9	6.9	0.9
S29	3.1	1.0	0.1	17.0	163076.2	3.7	6.2	1.7

Table 3
Summary table of sinkhole orientations and circularities at the last sampling date.

	Sinkhole orientation (°)	Stream bank orientation (°)	Sinkhole relative orientation (°)	Circularity index at the final time step
S1	*106*	*−17*	*123*	0.91
S2	*156*	*−17*	*173*	0.56
S3	*174*	*−17*	*191*	0.85
S4	*69*	*41*	*28*	0.93
S5	*134*	*41*	*93*	0.54
S6	*75*	*52*	*23*	0.77
S7	*33*	*28*	*5*	0.35
S8	*171*	*−28*	*199*	0.55
S9	*12*	*−28*	*40*	0.63
S10	*171*	*−28*	*199*	0.53
S11	*117*	*75*	*42*	0.94
S12	*68*	*75*	*7*	0.77
S13	*56*	*−20*	*76*	0.50
S14	*52*	*11*	*41*	0.75
S15	*4*	*11*	*7*	0.82
S16	*101*	*11*	*90*	0.91
S17	*10*	*11*	*1*	0.61
S18	*–33*	*3*	*35*	0.52
S19	*77*	*3*	*75*	0.73
S20	*105*	*106*	*1*	0.31
S21	*87*	*106*	*19*	0.77
S22	*114*	*106*	*8*	0.75
S23	*23*	*106*	*83*	0.49
S24	*120*	*137*	*17*	0.72
S25	*47*	*−60*	*107*	0.44
S26	*85*	*120*	*35*	0.34
S27	*53*	*40*	*13*	0.83
S28	*57*	*36*	*21*	0.83
S29	*8*	*87*	*79*	0.58

To summarize the section on area loss dynamics: seasonal changes in sinkhole area were correlated with individual storm rainfall depths rather than with accumulated seasonal rainfall (Table 1). The decadal data show that the timing of the rainfall event can play a major role in pipe collapse, as evidenced by the large seasonal differences in sinkhole area and area loss, and as shown by the coefficient of determination between rainfall depth and sinkhole area loss, including NDVI (Fig. 7).

4.2. Sinkhole morphology dynamics

The observed sinkholes had mainly elliptical morphology (Table 3). In the 2020 photos, 72% of the sinkholes showed a circularity index value < 0.80, which indicates elliptical morphology (see Fig. 3). Importantly, the sinkholes became more elliptical with time; the mean circularity index value in 2010 was 0.72, decreasing to 0.66 at the end of the measurement period in 2020.

The stereonet diagram in Fig. 8 displays the plane of the stream bank (N–S blue dashed line) and the lines of all of the sinkholes' major axes. Each line signifies the angle between a sinkhole's major axis and the stream bank's local orientation. Two groups of lines were distinguished: sub parallel to the stream bank and sub perpendicular to the stream bank (Fig. 8 and Table 3). Eight sinkholes were observed sub perpendicular to the stream bank ($65° < \text{angle} < 123°$), whereas 21 sinkholes were sub parallel ($-8° < \text{angle} < 42°$) to it. It is important to note that a similar dichotomous division was observed in the cracks' orientation on the soil surface, with many of the cracks parallel to the stream, a few of them perpendicular to it, and a very few in between.

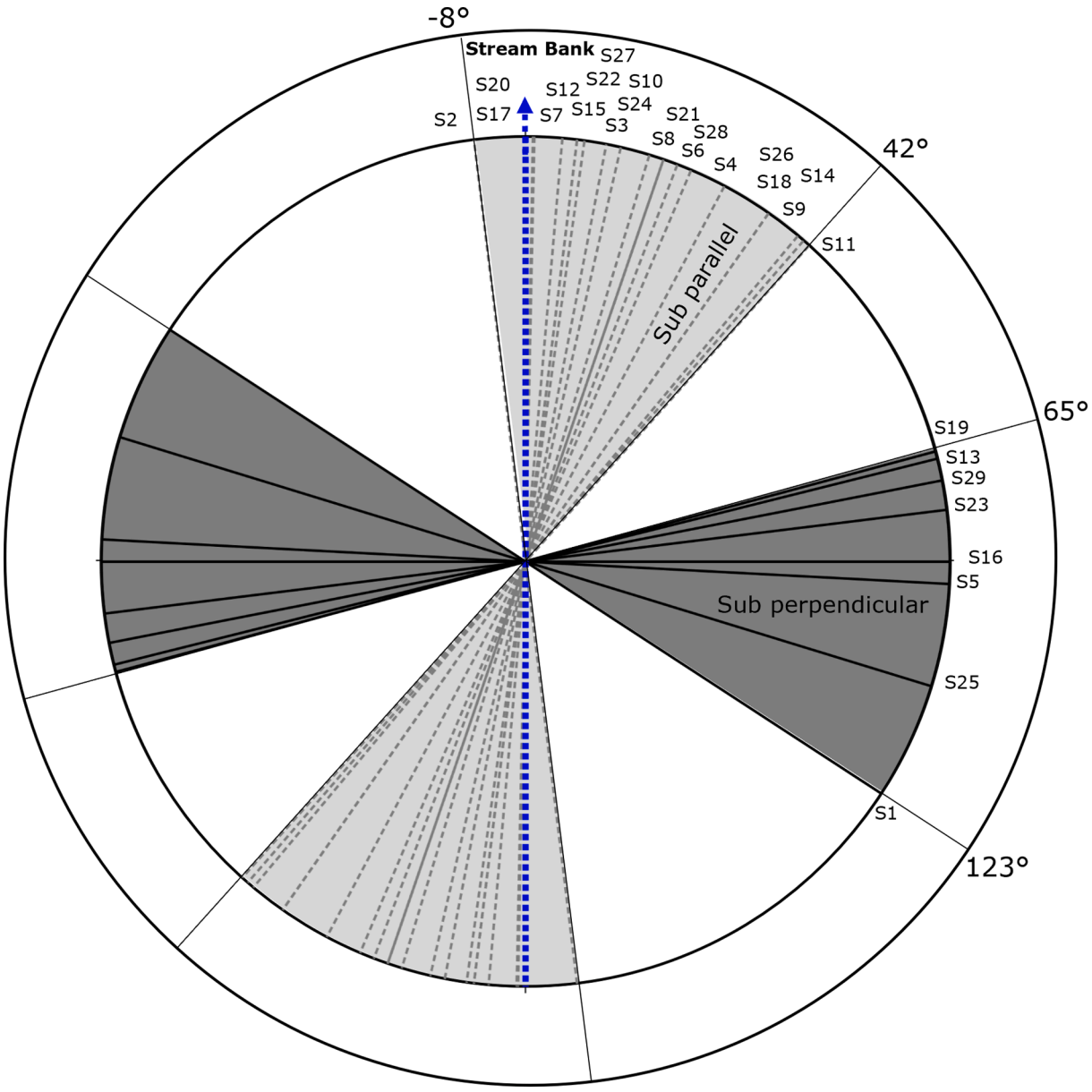

Fig. 8. Stereonet diagram of sinkhole orientations (major axis) relative to the stream bank. Dashed blue line represents the stream bank angle; black lines (dark gray background) represent sinkholes with sub perpendicular orientation to the stream bank (65° < angle < 123°), and dashed lines (light gray background) represent sinkholes with sub parallel orientation to the stream bank (-8° < angle < 42°). The morphology of the examined sinkholes showed development in a preferential orientation relative to the stream banks. (For interpretation of the references to colour in this figure legend, the reader is referred to the web version of this article.)

5. Discussion

5.1. Rate of change in sinkhole area on a seasonal scale

Increasing sinkhole area was correlated, in our data, with rainfall depth of extreme individual storms but not with accumulated seasonal rainfall depth (Table 1). This means that the rainfall effect on area loss by piping is intermittent and not cumulative. Our results from the northwestern Negev are compatible with those from a study applied under semi arid climatic conditions in Loess Plateau of China which reported a minor role for annually accumulated rainfall. However, short and intense rainfall events are responsible for the significant enlargement of existing sinkholes (Zhu, 2003). Similarly, other studies have also observed the effects of intense rainfall storms on the enlargement of sinkholes (Kariminejad et al., 2021; Pereyra et al., 2020), Additionally, the study conducted under dense vegetated temperate conditions in Poland revealed that short-term, yet intense events, cause significant geomorphological consequences (Bernatek-Jakiel et al., 2017). In contrast to less vegetated semi arid areas, under temperate conditions it was reported that most of the soil loss are mainly connected with the elongation of subsurface pipes and new pipe roof collapses, while enlargement of sinkholes delayed by vegetation (Bernatek-Jakiel et al., 2017). Indeed, despite the primary focus of these studies on soil loss, including the examination of collapsed features area and subsurface pipe widening (Verachtert et al., 2011), the consistent findings indicated a strong correlation between short and intense rainfall events and significant collapses, leading to immediately consequential enlargement of sinkholes especially under semi arid conditions. However, these previous piping studies relied on limited-time series and did not include extreme rainfall events in their analyses; therefore, there was no quantification of extreme rainfall events effects on seasonal area loss across a decade. Our study adds to current knowledge by relying on 10 seasons, and including the extreme “Alexa” storm event. This enabled comparing morphological sequences of extreme events and average rainfall events,

and revealing seasonal and interseasonal dynamics.

That said, the "Alexa" storm, which occurred at the beginning of the rainy season and had the largest rainfall depth and intensity in the previous five decades (184 mm, equal to 75% of the mean annual rainfall in 4 days), was accompanied by low temperatures and strong winds, resulting in severe floods (Israel Meteorological Service, n.d.). Correspondingly, our decadal data showed that > 37% of the sinkhole area enlarged during the "Alexa" storm itself.

Vegetation impacts a soil's resistance to water erosion due to stabilization of the topsoil by the fibrous root system (de Baets et al., 2006, 2008; Fox and Wilson, 2010; Gyssels et al., 2005; Torri et al., 2013). The role of vegetation in delaying the formation and growth of collapsing pipes in the Bieszczady Mountains (Bernatek, 2015; Bernatek-Jakiel and Wrońska-Wałach, 2018; Bernatek-Jakiel et al., 2017) and other regions (Hagerty, 1991; Löffler, 1974; Piccarreta et al., 2006; Romero Díaz and López Bermúdez, 1989) has been reported. In temperate zones, dense vegetation increases soil resistance, but it does not prevent subsurface erosion. Instead, it may only delay the enlargement of sinkholes that have formed underground. It has even been claimed that in temperate environments, subsurface erosion through piping may be more significant than surface erosion (Bernatek-Jakiel et al., 2017). The observed large seasonal difference in sinkhole area emphasizes the role of vegetation in pipe collapse in a semiarid environment as well; thus, vegetation amplifies the importance of rainfall timing due to large phenological differences throughout the season (Argaman et al., 2020).

Piping activity in the winter season may be hidden while the pipes are forming underground, waiting to collapse (Bernatek-Jakiel et al., 2017; Kariminejad et al., 2019; Wilson et al., 2018). Thus, collapse following a single storm event may reveal the previously hidden belowground activity of the piping system. Our data therefore show that rainfall timing and vegetation coverage can impact the likelihood and timing of pipe collapse in semiarid regions. Moreover, dry conditions combined with wetting and drying cycles, controlled by rainfall supply and high temperatures, can lead to the formation of soil cracks (Nahlieli et al., 2022; Pereyra et al., 2020). Extreme events early in the season might therefore explain the higher severity of area loss by piping in semiarid regions with badlands, such as those in Spain, Italy and Canada, compared to temperate regions (Verachtert et al., 2011).

In addition to the annual effect of "Alexa", we observed a decadal trend: the 2013–14 season was followed by several seasons of relative stability, possibly due to a lack of unstable material available for transportation after the mass collapse. On the catchment scale, however, area loss rate in the sinkholes did not show a clear trend. Soil pipe initiation was correlated with hillslope gradient and contributing area. However, these two variables did not show any correlation with the loss in sinkhole area. Lack of correlation with surface topography was also reported in Belgium (Verachtert et al., 2011). It is possible that local hydraulic gradients and subsurface contributing area, which influence pipe flow, do not necessarily equal soil surface topography (Wilson et al., 2015, 2017). Thus, even on steep, exposed hillslopes with low contributing areas, where there is a surface with potentially low water flow, soil pipes can develop due to desiccation cracking and subsurface preferential flow (Jones et al., 1997). Here, we added sinkhole location parameters (distance from stream bank and exposure to solar radiation) to the traditionally studied topographic threshold, to test the possible effect of tension cracks and stream bank parameters (height and gradient) on piping intensity (Faulkner et al., 2008; Nahlieli et al., 2022, 2023). However, no correlation was found between any of the parameters and area loss rate. Moreover, many sinkholes showed a change in area despite their small contributing area.

Area loss over time by piping in semiarid regions is a dynamic process and according to our data, it can vary on both seasonal and decadal scales. Rainfall regime and vegetation cover, dry spells and intense rainfall events, such "Alexa", in the early stages of winter when vegetation has not yet developed can cause irreversible damage and have a significant geometrical effect. These factors should be considered when assessing soil erosion from agricultural catchments of loess-dominated landscapes. These temporal factors are particularly important given the large extent of loess soils worldwide (e.g., the European Loess Belt and the Chinese Loess Plateau).

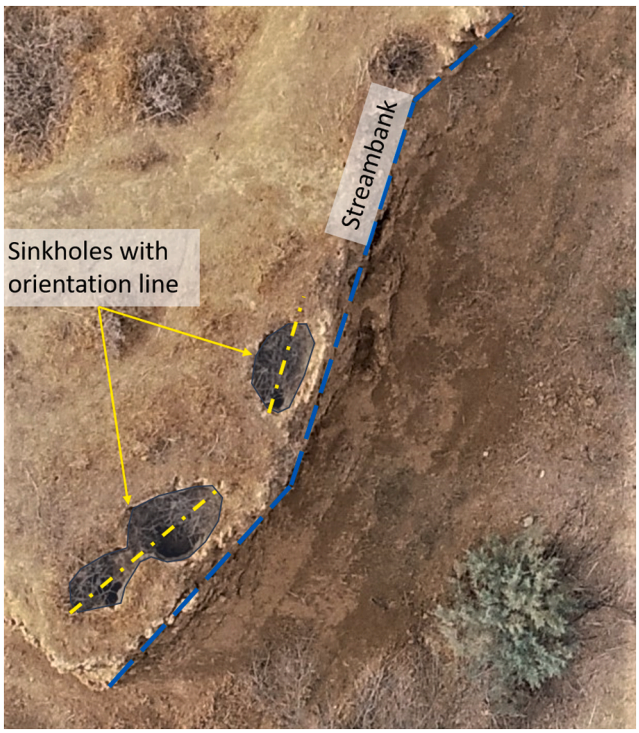

Fig. 9. Piping system developed on stream banks at the study site. A drone image of developed piping sinkholes with orientation parallel to the stream bank.

5.2. Soil piping and sinkhole morphology

In the past, sinkholes have been studied mainly in terms of area and volume estimations (Kariminejad et al., 2022; Verachtert et al., 2011). However, studies that did report on sinkhole shape and geometry indicated mainly two groups of sinkhole morphology. The first consists of circular sinkholes characterized by a deep chimney-like shape, found in marl lithology and saline soils (Faulkner, 2013; Faulkner et al., 2000; Hamawi et al., 2022). The reason for the circular form in these environments is the high solubility of these soils and the lower dependence on preferential lines and soil cracks (Greve et al., 2010; Wilson et al., 2008). Moreover, the soil profile in those studies is very deep (on the order of meters), decreasing the influence of cavity direction in the subsurface. The second group is characterized by elongated sinkholes. For example, in the work of Faulkner et al. 2008 in Southern Italy, and Bernatek-Jakiel and Poesen (2018) in Belgium, Ethiopia, Spain and Poland in agricultural lands and rangelands, the sinkholes in the published ground photographs clearly look elongated. Those studies refer mainly to clayish and loess soils that more typically have subsurface soil cracks. Namely, the underlying infrastructure and hydraulic gradient in those soils may affect the sinkhole shape on the surface.

Previous studies have shown that sinkhole elongation may be affected by pre-existing macropores, such as neotectonic joints, tension cracks, root channels, desiccation cracks and animal burrows (Piccarreta et al., 2006; Verachtert et al., 2010). Furthermore, the conceptual model of Nahlieli et al. (2022) claims that the tension cracks in the stream bank act as a catalyst for the development of piping sinkholes that run parallel to the bank. These cracks can act as a preferential line to the subsurface flow of the pipes and therefore may control the direction of the sinkhole's collapse. At our site, 72% of the sinkholes were elliptical and 72%

were oriented sub parallel to stream bank (Fig. 9). In addition, many of the sinkholes became even more elliptical, as reflected by the decreasing circularity index over time. These results partially support the assertion that soil cracks in the subsurface dictate the direction of the below-surface pipes.

The implications of sinkhole orientation with reference to the stream bank are even more complex. Only a few papers have studied piping network morphology in terms of orientation (Bernatek-Jakiel et al., 2019; Faulkner, 2013; Pereyra et al., 2020). These studies reported that in most cases, sinkhole orientation tends to follow the hydraulic gradient and soil pipes are aligned to the downslope surface orientation (Bernatek-Jakiel et al., 2019; Pereyra et al., 2020). However, none of these studies related the orientation of the elongated collapsed features to the stream bank. Such dominance of the developing orientation near the stream bank may help to better understand the stream bank's linkage to the evolution of soil pipes. This is because the primary process of piping includes the development of soil tension cracks due to proximity to the stream banks, playing a decisive role as preferential flow paths (Nahlieli et al., 2022).

We have to emphasize that the presented sinkhole data on piping dynamics and pipe morphology has limitations. Soil pipes are not linear—they may meander horizontally and vertically (Bernatek-Jakiel et al., 2017); moreover, a time series analysis of roof collapses reveals area loss, and not volumetric soil loss, which is caused by subsurface water flow. We used area loss here as a proxy to soil loss. Data were obtained from the aerial photographs, hence, ongoing underground piping erosion was not included in the soil loss estimation. Pipe collapse is a sequence of subsurface erosion that was not visible until the roof collapsed.

6. Conclusions

Monitoring spatiotemporal sinkhole dimension dynamics during the course of a decade in the northwestern Negev revealed the following insights regarding piping development in semiarid regions: (1) large rainfall events, such as the "Alexa" storm, have a much larger effect on area loss from sinkholes in semiarid regions than the cumulative effect of small rainfall events; (2) the timing of these large rainfall events during the season is very important; in the early stages of winter, area loss from sinkholes is larger due to absence of a defensive shield effect of herbaceous vegetation; (3) it takes time to produce soil material that is then available for transportation; therefore, if two large events occur one after the other, the second is not expected to result in large area losses; (4) most of the sinkholes in the study area were elliptical, possibly related to subsurface flow lines and crack systems that develop in the loess environment; (5) a notable morphological feature of sinkhole development is related to stream bank soil cracking in accordance with tension crack orientation; and finally (6) this study draws attention to the need for more research to better identify the factors that affect piping rates and the hydrological connectivity dictated by tension stress in stream banks.

Funding

This work was supported by the Chief Scientist of the Ministry of Agriculture & Rural Development [grant number 16-17-0005, 2022].

Declaration of Competing Interest

The authors declare the following financial interests/personal relationships which may be considered as potential competing interests: Osher Rafaeli reports financial support was provided by Israeli Ministry of Agriculture & Rural Development.

Data availability

The authors are unable or have chosen not to specify which data has been used.

References

Argaman, E., Barth, R., Moshe, Y., Ben-Hur, M., 2020. Long-term effects of climatic and hydrological variation on natural vegetation production and characteristics in a semiarid watershed: the northern Negev, Israel. Sci. Tot. Environ. 747 https://doi.org/10.1016/j.scitotenv.2020.141146.

Barendregt, R.W., Ongley, E.D., 1977. Piping in the Milk River Canyon, southeastern Alberta - a contemporary dryland geomorphic process, in: Erosion and Solid Material Transport in Inland Waters. Symposium / convened jointly by UNESCO and IAHS. International Association of Hydrological Sciences Publication 122, pp. 233–243.

Bernatek, A., 2015. The influence of piping on mid-mountain relief: a case study from the Polish Bieszczady Mts. (Eastern Carpathians). Carpathian J. Earth Environ. Sci. 10, 107–120.

Bernatek-Jakiel, A., Bruthans, J., Vojtíšek, J., Stolarczyk, M., Zaleski, T., 2020. Sediment detachment in piping-prone soils: Cohesion sources and potential weakening mechanisms. Earth Surf. Process. Landforms 45, 3185–3201. https://doi.org/10.1002/esp.4959.

Bernatek-Jakiel, A., Poesen, J., 2018. Subsurface erosion by soil piping: significance and research needs. Earth-Sci. Rev. https://doi.org/10.1016/j.earscirev.2018.08.006.

Bernatek-Jakiel, A., Wrońska-Wałach, D., 2018. Impact of piping on gully development in mid-altitude mountains under a temperate climate: a dendrogeomorphological approach. Catena 165, 320–332. https://doi.org/10.1016/j.catena.2018.02.012.

Bernatek-Jakiel, A., Jakiel, M., Krzemień, K., 2017. Piping dynamics in mid-altitude mountains under a temperate climate: Bieszczady Mountains, eastern Carpathians. In: Earth Surface Processes and Landforms. John Wiley and Sons, New York, pp. 1419–1433. https://doi.org/10.1002/esp.4160.

Bernatek-Jakiel, A., Gutiérrez, F., Nadal-Romero, E., Jakiel, M., 2019. Exploring the frequency-size relationships of pipe collapses in different morphoclimatic regions. Geomorphology 345. https://doi.org/10.1016/j.geomorph.2019.106845.

Cai, Q.-G., 2001. Soil erosion and management on the Loess Plateau. J. Geograph. Sci. 11, 53–70.

Castillo, C., Gómez, J.A., 2016. A century of gully erosion research: Urgency, complexity and study approaches. Earth-Sci. Rev. 160, 300–319. https://doi.org/10.1016/j.earscirev.2016.07.009.

Chen, Y., Chen, W., Janizadeh, S., Bhunia, G.S., Bera, A., Pham, Q.B., Linh, N.T.T., Balogun, A.L., Wang, X., 2022. Deep learning and boosting framework for piping erosion susceptibility modeling: spatial evaluation of agricultural areas in the semi-arid region. Geocarto Int. 37, 4628–4654. https://doi.org/10.1080/10106049.2021.1892212.

Cohen, S., Svoray, T., Sela, S., Hancock, G., Willgoose, G., 2017. Soilscape evolution of aeolian-dominated hillslopes during the Holocene: investigation of sediment transport mechanisms and climatic-anthropogenic drivers. Earth Surf. Dynam. 5, 101–112. https://doi.org/10.5194/esurf-2016-4.

de Baets, S., Poesen, J., Gyssels, G., Knapen, A., 2006. Effects of grass roots on the erodibility of topsoils during concentrated flow. Geomorphology 76, 54–67. https://doi.org/10.1016/j.geomorph.2005.10.002.

de Baets, S., Poesen, J., Reubens, B., Wemans, K., de Baerdemaeker, J., Muys, B., 2008. Root tensile strength and root distribution of typical Mediterranean plant species and their contribution to soil shear strength. Plant and Soil 305, 207–226. https://doi.org/10.1007/s11104-008-9553-0.

de Ploey, J., Moeyersons, J., Goossens, D., 1995. The De Ploey erosional susceptibility model for catchments. Catena 25, 269–314. https://doi.org/10.1016/0341-8162(95)00014-J.

Faulkner, H., 2013. Badlands in marl lithologies: a field guide to soil dispersion, subsurface erosion and piping-origin gullies. Catena 106, 42–53. https://doi.org/10.1016/j.catena.2012.04.005.

Faulkner, H., Spivey, D., Alexander, R., 2000. The role of some site geochemical processes in the development and stabilisation of three badland sites in Almeria, Southern Spain. Geomorphology 35, 87–99. https://doi.org/10.1016/S0169-555X(00)00024-6.

Faulkner, H., Alexander, R., Zukowskyj, P., 2008. Slope–channel coupling between pipes, gullies and tributary channels in the Mocatán catchment badlands, Southeast Spain. Earth Surf. Process. Landforms. 33, 1242–1260. https://doi.org/10.1002/esp.1610.

Fox, G.A., Wilson, G.V., 2010. The role of subsurface flow in hillslope and stream bank erosion: A review. Soil Sci. Soc. Am. J. 74, 717–733. https://doi.org/10.2136/sssaj2009.0319.

García-Ruiz, J.M., 2010. The effects of land uses on soil erosion in Spain: a review. Catena 81. https://doi.org/10.1016/j.catena.2010.01.001.

Greve, A., Andersen, M.S., Acworth, R.I., 2010. Investigations of soil cracking and preferential flow in a weighing lysimeter filled with cracking clay soil. J. Hydrol. 393, 105–113. https://doi.org/10.1016/j.jhydrol.2010.03.007.

Gutiérrez, M., Sancho, C., Benito, G., Sirvent, J., Desir, G., 1997. Quantitative study of piping processes in badland areas of the Ebro Basin, NE Spain. Geomorphology 20, 237–253. https://doi.org/10.1016/S0169-555X(97)00026-3.

Gyssels, G., Poesen, J., Bochet, E., Li, Y., 2005. Impact of plant roots on the resistance of soils to erosion by water: a review. Prog. Phys. Geogr. Earth Environ. 29 https://doi.org/10.1191/0309133305 pp443ra.

Hagerty, D.J., 1991. Piping/sapping erosion. II: Identification-diagnosis. J. Hydraul. Eng. 117 https://doi.org/10.1061/(ASCE)0733-9429(1991)117:8(1009).

Hamawi, M., Goren, L., Mushkin, A., Levi, T., 2022. Rectangular drainage pattern evolution controlled by pipe cave collapse along clastic dikes, the Dead Sea Basin, Israel. Earth Surf. Process. Landforms. 47, 936–954. https://doi.org/10.1002/esp.5295.

Hochman, A., Scher, S., Quinting, J., Pinto, J.G., Messori, G., 2022. Dynamics and predictability of cold spells over the Eastern Mediterranean. Clim. Dyn. 58, 2047–2064. https://doi.org/10.1007/s00382-020-05465-2.

Hoober, D., Svoray, T., Cohen, S., 2017. Using a landform evolution model to study ephemeral gullying in agricultural fields: the effects of rainfall patterns on ephemeral gully dynamics. Earth Surf. Process. Landforms 42, 1213–1226. https://doi.org/10.1002/esp.4090.

[dataset] Israel Meteorological Service, n.d. https://ims.data.gov.il/he/ims-results.

Jones, J.A.A., 2004. Implications of natural soil piping for basin management in upland Britain. Land Degrad. Develop. 15, 325–349. https://doi.org/10.1002/ldr.618.

Jones, J.A.A., Cottrell, C.I., 2007. Long-term changes in stream bank soil pipes and the effects of afforestation. J. Geophys. Res. - Earth Surf. 112 https://doi.org/10.1029/2006JF000509.

Jones, J.A.A., Richardson, J.M., Jacob, H.J., 1997. Factors controlling the distribution of piping in Britain: a reconnaissance. Geomorphology 20, 289–306. https://doi.org/10.1016/S0169-555X(97)00030-5.

Kariminejad, N., Hosseinalizadeh, M., Pourghasemi, H.R., Bernatek-Jakiel, A., Campetella, G., Ownegh, M., 2019. Evaluation of factors affecting gully headcut location using summary statistics and the maximum entropy model: Golestan Province, NE Iran. Sci. Tot. Environ. 677, 281–298. https://doi.org/10.1016/j.scitotenv.2019.04.306.

Kariminejad, N., Hosseinalizadeh, M., Pourghasemi, H.R., Tiefenbacher, J.P., 2021. Change detection in piping, gully head forms, and mechanisms. Catena 206. https://doi.org/10.1016/j.catena.2021.105550.

Kariminejad, N., Shariati, M., Hosseinalizadeh, M., Pourghasemi, H.R., Maleki, S., 2022. Investigating geometrical characteristics of collapsed pipes and the changing role of driving factors. J. Environ. Manage. 312, 114910 https://doi.org/10.1016/j.jenvman.2022.114910.

Kariminejad, N., Sepehr, A., Poesen, J., Hassanli, A., 2023. Combining UAV remote sensing and pedological analyses to better understand soil piping erosion. Geoderma 429. https://doi.org/10.1016/j.geoderma.2022.116267.

Kobal, M., Bertoncelj, I., Pirotti, F., Dakskobler, I., Kutnar, L., 2015. Using lidar data to analyse sinkhole characteristics relevant for understory vegetation under forest cover – case study of a high karst area in the Dinaric mountains. PLoS One. 10.

Li, X.A., Wang, L., Hong, B., Li, L.C., Liu, J., Lei, H.N., 2020. Erosion characteristics of loess tunnels on the Loess Plateau: a field investigation and experimental study. Earth Surf. Process. Landforms. 45, 1945–1958. https://doi.org/10.1002/esp.4857.

Löffler, E., 1974. Piping and pseudokarst features in the tropical lowlands of New Guinea (Röhrenerosion und Pseudokarsterscheinungen im tropischen Tiefland). Erdkunde 28, 13–18.

Masek, J.G., Vermote, E.F., Saleous, N.E., Wolfe, R., Hall, F.G., Huemmrich, K.F., Gao, F., Kutler, J., Lim, T.K., 2006. A Landsat surface reflectance dataset for North America, 1990–2000. IEEE Geosci. Remote Sens. Lett. 3, 68–72. https://doi.org/10.1109/LGRS.2005.857030.

Nachshon, U., 2016. Seepage weathering impacts on erosivity of arid stream banks: a new conceptual model. Geomorphology 261, 212–221. https://doi.org/10.1016/j.geomorph.2016.03.011.

Nagy, B., Szákal, S., 2020. Measuring the circularity of congressional districts. Soc. Econ. 42, 298–312. https://doi.org/10.1556/204.2020.00008.

Nahlieli, A., Svoray, T., Argaman, E., 2022. Piping formation and distribution in the semi-arid Northern Negev environment: a new conceptual model. Catena 213, 106201. https://doi.org/10.1016/j.catena.2022.106201.

Nahlieli, A., Svoray, T., Argaman, E., 2023. Mapping areas prone to piping using random forest with key explanatory variables. Geoderma 431. https://doi.org/10.1016/j.geoderma.2023.116367.

Panagos, P., Katsoyiannis, A., 2019. Soil erosion modelling: the new challenges as the result of policy developments in Europe. Environ. Res. 172, 470–474. https://doi.org/10.1016/j.envres.2019.02.043.

Parker, G.G., Jenne, E.A., 1967. Structural failure of western highways caused by piping. Symposium on Subsurface Drainage, Washington DC, pp. 57–76.

Pereyra, M.A., Fernández, D.S., Marcial, E.R., Puchulu, M.E., 2020. Agricultural land degradation by piping erosion in Chaco Plain, Northwestern Argentina. Catena 185. https://doi.org/10.1016/j.catena.2019.104295.

Piccarreta, M., Faulkner, H., Bentivenga, M., Capolongo, D., 2006. The influence of physico-chemical material properties on erosion processes in the badlands of Basilicata, Southern Italy. Geomorphology 81, 235–251. https://doi.org/10.1016/j.geomorph.2006.04.010.

Poesen, J., Leuven, K.U., van Wesemael, B., 1996. Contribution of gully erosion to sediment production in cultivated lands and rangelands. Erosion and Sediment Yield: Global and Regional Perspectives (Proceedings of the Exeter Symposium). IAHS Publ. no. 236, pp. 251–266.

Poesen, J., Nachtergaele, J., Verstraeten, G., Valentin, C., 2002. Gully erosion and environmental change: importance and research needs. Catena 50, 91–133. https://doi.org/10.1016/S0341-8162(02)00143-1.

Poesen, J., 2011. Challenges in gully erosion research, Landform Analysis.

Polsby, D.D., Popper, R.D., 1991. The third criterion: compactness as a procedural safeguard against partisan gerrymandering. Yale Law Policy Rev. 9, 301–353.

Rinot, O., Levy, G.J., Steinberger, Y., Svoray, T., Eshel, G., 2019. Soil health assessment: a critical review of current methodologies and a proposed new approach. Sci. Tot. Environ. 648, 1484–1491. https://doi.org/10.1016/j.scitotenv.2018.08.259.

Romero Díaz, A., Plaza Martínez, J., Sánchez Soriano, A., Belmonte Serrato, F., Ruiz Sinoga, J., 2009. Estimated volume of soil lost by piping erosion processes. Southeastern Spain.

Romero Díaz, A., López Bermúdez, F., 1989. Piping erosion and badland development in South-East Spain. Catena Suppl. 14, 59–73.

Starkel, L., 2011. Paradoxes in the development of gullies. Landform Anal. 17, 11–13.

Stavi, I., Argaman, E., 2016. Soil quality and aggregation in runoff water harvesting forestry systems in the semi-arid Israeli Negev. Catena 146, 88–93. https://doi.org/10.1016/j.catena.2016.06.010.

Svoray, T., Michailov, E., Cohen, A., Rokach, L., Sturm, A., 2012. Predicting gully initiation: Comparing data mining techniques, analytical hierarchy processes and the topographic threshold. Earth Surf. Process. Landforms 37, 607–619.

Svoray, T., Shoshany, M., 2004. Multi-scale analysis of intrinsic soil factors from SAR-based mapping of drying rates. Remote Sens. Environ. 92, 233–246. https://doi.org/10.1016/j.rse.2004.06.011.

Svoray, T., 2022. A Geoinformatics Approach to Water Erosion, A Geoinformatics Approach to Water Erosion – Soil Loss and Beyond. Springer International Publishing, Cham.

Torri, D., Santi, E., Marignani, M., Rossi, M., Borselli, L., MacCherini, S., 2013. The recurring cycles of *biancana* badlands: erosion, vegetation and human impact. Catena 106, 22–30. https://doi.org/10.1016/j.catena.2012.07.001.

Uri, N.D., Lewis, J.A., 1998. The dynamics of soil erosion in US agriculture. Sci. Tot. Environ. 218, 45–58. https://doi.org/10.1016/S0048-9697(98)00198-3.

Valentin, C., Poesen, J., Li, Y., 2005. Gully erosion: impacts, factors and control. Catena 63, 132–153. https://doi.org/10.1016/j.catena.2005.06.001.

Vanmaercke, M., Panagos, P., Vanwalleghem, T., Hayas, A., Foerster, S., Borrelli, P., Rossi, M., Torri, D., Casali, J., Borselli, L., Vigiak, O., Maerker, M., Haregeweyn, N., de Geeter, S., Zgłobicki, W., Bielders, C., Cerdà, A., Conoscenti, C., de Figueiredo, T., Evans, B., Golosov, V., Ionita, I., Karydas, C., Kertész, A., Krása, J., le Bouteiller, C., Radoane, M., Ristić, R., Rousseva, S., Stankoviansky, M., Stolte, J., Stolz, C., Bartley, R., Wilkinson, S., Jarihani, B., Poesen, J., 2021. Measuring, modelling and managing gully erosion at large scales: a state of the art. Earth-Sci. Rev. 218 https://doi.org/10.1016/j.earscirev.2021.103637.

Verachtert, E., van den Eeckhaut, M., Poesen, J., Deckers, J., 2010. Factors controlling the spatial distribution of soil piping erosion on loess-derived soils: a case study from central Belgium. Geomorphology 118, 339–348. https://doi.org/10.1016/j.geomorph.2010.02.001.

Verachtert, E., Maetens, W., van den Eeckhaut, M., Poesen, J., Deckers, J., 2011. Soil loss rates due to piping erosion. Earth Surf. Process. Landforms 36, 1715–1725. https://doi.org/10.1002/esp.2186.

Vermote, E., Justice, C., Claverie, M., Franch, B., 2016. Preliminary analysis of the performance of the Landsat 8/OLI land surface reflectance product. Remote Sens. Environ. 185, 46–56. https://doi.org/10.1016/j.rse.2016.04.008.

Wilson, G.V., Cullum, R.F., Römkens, M.J.M., 2008. Ephemeral gully erosion by preferential flow through a discontinuous soil-pipe. Catena 73, 98–106. https://doi.org/10.1016/j.catena.2007.09.008.

Wilson, G.V., Rigby, J.R., Dabney, S.M., 2015. Soil pipe collapses in a loess pasture of Goodwin Creek watershed, Mississippi: role of soil properties and past land use. Earth Surf. Proc. Landforms 40, 1448–1463. https://doi.org/10.1002/esp.3727.

Wilson, G.V., Nieber, J.L., Fox, G.A., Dabney, S.M., Ursic, M., Rigby, J.R., 2017. Hydrologic connectivity and threshold behavior of hillslopes with fragipans and soil pipe networks. Hydrol. Proc. 31, 2477–2496. https://doi.org/10.1002/hyp.11212.

Wilson, G.V., Wells, R., Kuhnle, R., Fox, G., Nieber, J., 2018. Sediment detachment and transport processes associated with internal erosion of soil pipes. Earth Surf. Process. Landforms 43, 45–63. https://doi.org/10.1002/esp.4147.

Wolman, M.G., Gerson, R., 1978. Relative scales of time and effectiveness of climate in watershed geomorphology. Earth Surf. Process. Landforms 3, 189–208. https://doi.org/10.1002/esp.3290030207.

Yair, A., Kossovsky, A., 2002. Climate and surface properties: hydrological response of small arid and semi-arid watersheds. Geomorphology 42, 43–57. https://doi.org/10.1016/S0169-555X(01)00072-1.

Zhao, G., Mu, X., Wen, Z., Wang, F., Gao, P., 2013. Soil erosion, conservation, and eco-environment changes in the Loess Plateau of China. Land Degrad. Develop. 24, 499–510. https://doi.org/10.1002/ldr.2246.

Zhu, T.X., 2003. Tunnel development over a 12 year period in a semi-arid catchment of the Loess Plateau, China. Earth Surf. Process. Landforms 28, 507–525. https://doi.org/10.1002/esp.455.

Zhu, T.X., 2012. Gully and tunnel erosion in the hilly Loess Plateau region, China. Geomorphology 153–154, 144–155. https://doi.org/10.1016/j.geomorph.2012.02.019.